

# SP: An Advanced Surface-Potential-Based Compact MOSFET Model (invited)

G. Goldenblat, T.-L. Chen, X. Gu, H. Wang and X. Cai

Department of Electrical Engineering, The Pennsylvania State University,  
University Park, PA 16802, USA, goldenblat@psu.edu

## Abstract

This work describes an advanced physics-based compact MOSFET model (SP). Both the quasi-static and non-quasi-static versions of SP are surface-potential-based. The model is symmetric, includes the accumulation region, small-geometry effects, and has a consistent current and charge formulation. The surface potential is computed analytically and there are no iterative loops anywhere in the model. Availability of the surface potential in the source-drain overlap regions enables a physics-based formulation of the extrinsic model (e.g. gate tunneling current) and allows for a noise model free of discontinuities or unphysical interpolation schemes. Simulation results are used to illustrate the interplay between the model structure and circuit design.

## Introduction: Selecting the Model Structure

**T**HIS work introduces the latest and most advanced surface-potential-based model called SP. The emphasis is on the interplay between the device physics and circuit simulation. The relation between the model structure and circuit simulation is both subtle and consequential. For example, using a source-referenced threshold voltage,  $V_{th}$ , makes it impossible to model R2R circuits, while the popular textbook expression for the velocity saturation leads to a singularity in the  $I_d(V_{ds})$  curve for  $V_{ds} = 0$  with obvious negative consequences for analog circuit design. It is then important to determine a desirable model structure for next generation compact models. At present, there are essentially three possibilities:  $V_{th}$ -based,  $q_i$ -based and  $\phi_s$ -based models ( $q_i$ -inversion charge,  $\phi_s$ -surface potential). The limitations of the familiar  $V_{th}$ -based approach are well documented [1], [2]. They stem from the inevitable unphysical nature of  $V_{th}$ -based models in the transition regions such as between subthreshold and strong inversion. As the power supply voltage is reduced, the transition regions become a significant fraction of the voltage swing, essentially invalidating a  $V_{th}$ -based approach.

The  $q_i$ -based approach was introduced in [3], [4], developed in [5]–[7], rediscovered in [8] and presented once again in [9]. Central to this method is the “inversion charge relation”

$$(q_i/n) + \phi_t \ln(q_i/n\phi_t) = (V_{gb} - V_{fb})/n - \phi_n - n_1 \quad (1)$$

where  $q_i$  is normalized to  $C_{ox}$ ,  $V_{fb}$  denotes the flat-band voltage,  $\phi_n$  is the imref splitting and coefficients  $n$ ,  $n_1$  are position-independent in the MOSFET channel. In view of the approximate nature of (1), various definitions, interpretations and expressions for  $n$  and  $n_1$  are available in the literature. By using (1)  $q_i$ -based models allow for a simultaneous and mostly

physical modeling of the subthreshold and strong inversion regions. However, in the development of SP, the inversion charge relation was rejected in favor of the  $\phi_s$ -based approach for the following reasons. First, using (1) precludes physical modeling of the accumulation region (essential for varactor modeling). This implies the regional nature of a  $q_i$ -based model with undesirable consequences so familiar to both users and developers from  $V_{th}$ -based work. Second, even in its area of validity ( $\phi_s \geq 3\phi_t$ ,  $\phi_t = kT/q$ ) relation (1) is an approximation of the more accurate result (see below)

$$q_i + q_b + \phi_t \ln \left[ \frac{q_i(q_i + 2q_b)}{\gamma^2 \phi_t} \right] = V_{gb} - V_{fb} - \phi_n - 2\phi_b \quad (2)$$

where  $q_b$  is the bulk charge normalized similarly to  $q_i$ . Consequently, it does not seem worthwhile to base a MOSFET model on an approximate solution of (1) which is an approximation of (2) which itself is an approximate form of the general surface-potential equation obtained by neglecting the contributions of majority carriers. Finally,  $\phi_s$  and not just  $q_i$  is needed in the development of the extrinsic MOSFET model (e.g. gate current, noise model).

This leaves a  $\phi_s$ -based model structure as a natural choice for the next generation compact MOSFET models. Several  $\phi_s$ -based compact models have been developed and successfully implemented [10]–[13]. This approach is well recognized as both the most physical and the most difficult to implement. The development of SP is enabled by new accurate approximate solutions of several mathematical problems retarding the progress of  $\phi_s$ -based models.

## General Features of SP

These can be summarized as follows:

- $\phi_s$ -based, substrate referenced
- Analytic (non-iterative) computation of  $\phi_s$  from accumulation to inversion
- Symmetric with respect to source-drain interchange, no  $d^2 I_d / dV_{ds}^2$  singularity
- Physically based modeling of small-geometry effects via lateral field gradient
- DC, quasi-static (QS) and non-quasi-static (NQS) models are consistent
- Accumulation region modeling is physics-based
- $\phi_s$ -based modeling of the overlap regions
- Physics-based gate and substrate current models
- Simple expressions for key variables in all regions of operation, obtained using “symmetric linearization” concept
- Benchmark tests are automatically satisfied with no special effort

- Quantum mechanical effects and polysilicon depletion
- Thermal, 1/f and channel-induced gate noise models; “Excessive” thermal noise is physically modeled

### Computation of the Surface Potential

The key problem is that  $\phi_s$  is an implicit function of the gate bias and  $\phi_n$  [14]:

$$(V_{gb} - V_{fb} - \phi_s)^2 = \gamma^2 \phi_t [(e^{-x} + x - 1) + \Delta_n (e^x - x - 1)] \quad (3)$$

where  $x = \phi_s / \phi_t$  and  $\Delta_n = \exp[-(2\phi_b + \phi_n) / \phi_t]$ .

Eq. (3) describes all regions of MOSFET operation but has no closed-form solution. Neither does its simplified version valid for  $\phi_s \geq 3\phi_t$  (ignoring the accumulation region) [15]:

$$[(V_{gb} - V_{fb} - \phi_s) / \gamma]^2 = \phi_s + \phi_t \Delta \quad (4)$$

where  $\Delta = \exp[(\phi_s - 2\phi_b - \phi_n) / \phi_t]$ . This often necessitates an iterative solution for  $\phi_s(V_{gb}, \phi_n)$ . We note in passing that using charge-sheet model (CSM) equations  $q_b = \gamma\sqrt{\phi_s}$  and  $q_i = \gamma\sqrt{\phi_s + \phi_t\Delta} - q_b$  yields  $q_i = \gamma^2\phi_t\Delta / (q_i + 2q_b)$  which is equivalent to (2) but not to (1). Thus the occasional claim that one can solve equation for the surface potential in terms of numerically evaluated “Lambert function” (solution  $W(x)$  of  $We^W = x$ ) by reformulating (4) in terms of  $q_i$  is not valid. Only an approximation (1) can be dealt with in this manner.

The search for an approximate analytical solution of (4) was initiated in [16] using smoothing functions to connect asymptotic solutions of (4) in subthreshold and strong inversion. Naturally, even the best approximations of this type [11] have an accuracy of 2-3mV which is not sufficient for modelling of transconductances and transcapacitances. By using a different approach one can obtain an approximate solution of eq. (3) with an accuracy better than 1nV [17]. A generalization of this method given in Appendix A leads to an approximate solution of the complete surface potential, eq. (3). As shown in Fig. 1, the accuracy of the new algorithm is the same as that in [17], but now the accumulation region is included. This obviates the need to develop a separate model of the accumulation region which is an unfortunate but inevitable feature of  $q_i$ -based models.

In the development of the extrinsic  $\phi_s$ -based model it is often necessary to find the surface potential  $\phi_{ov}$  in the heavily doped source and drain overlap regions. In these regions the minority carrier contribution to the charge density is negligible, and instead of the general eq. (3) one only needs a simplified version obtained by omitting the term  $\Delta_n(e^x - x - 1)$ . The analytical approximation for  $\phi_s$  in this case is even simpler than the one given in Appendix A. Typical results are shown in Fig. 2, indicating an accuracy of better than  $10^{-10}$ V.

### Intrinsic SP: $I_d$ and Terminal Charges

Most compact models use linearization of the bulk charge as a function of  $\phi_s$ . To preserve the model symmetry with respect to source-drain interchange, in SP this linearization is introduced as

$$q_b(\phi_s) = q_b(\phi_m) + (dq_b/d\phi_s)_{\phi_s=\phi_m} (\phi_s - \phi_m) \quad (5)$$

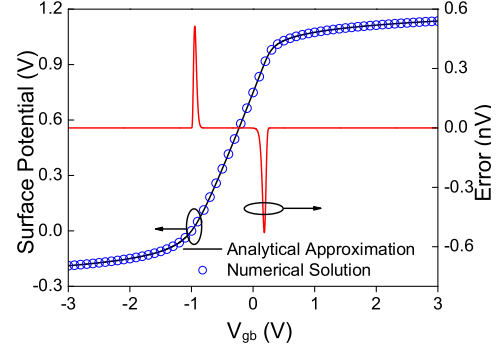


Fig. 1. Comparison of the analytical approximation of the surface potential in the channel area with numerical solution;  $N_{sub} = 5 \times 10^{17} \text{cm}^{-3}$ ,  $t_{ox} = 25 \text{\AA}$ ,  $V_{fb} = -1.0 \text{V}$  and  $T = 300 \text{K}$

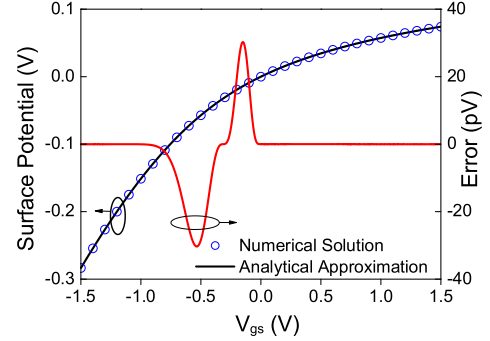


Fig. 2. Comparison of the analytical approximation of the surface potential in the overlap regions with numerical solution;  $N_{ov} = 5 \times 10^{19} \text{cm}^{-3}$ ,  $t_{ox} = 20 \text{\AA}$ ,  $V_{fb} = 0$  and  $T = 300 \text{K}$

where  $\phi_m = (\phi_{ss} + \phi_{sd})/2$  and  $\phi_{ss}, \phi_{sd}$  are the values of  $\phi_s$  at the source and drain ends of the channel. Consequently, the inversion charge  $q_i = q_{im} - \alpha(\phi_s - \phi_m)$ , where  $q_{im}$  is the inversion charge at the “potential midpoint”,  $\phi_s = \phi_m$ , and the linearization coefficient  $\alpha = 1 + \gamma/2\sqrt{\phi_m}$ . Apart from preserving the Gummel symmetry, this technique has several advantages. First, the coefficients  $a_1, a_2$  in the traditional formulation [18] are eliminated. Second, the resulting version of the CSM is numerically identical to the original one [15] but has significantly simpler expressions for the drain current and the terminal charges [19]. Finally, a simple  $\phi_s(y)$  expression can be obtained explicitly which is essential in the development of noise and gate current models and for NQS formulation.

When combined with the CSM version of the drift-diffusion equation, symmetric linearization yields [13]

$$I_d = \beta(q_{im} + \alpha\phi_t)\phi(r_L + \delta_0\phi/V_c)^{-1} \quad (6)$$

where  $\beta = \mu(W/L)C_{ox}$ ,  $V_c = E_cL$ ,  $E_c$  is the critical field,  $r_L = (1 + \Delta L_{CLM}/L)^{-1}$  and  $\Delta L_{CLM}$  models channel length modulation. Variable  $\delta_0$  is introduced to sharpen the drift velocity dependence on the lateral field [20]. In SP,  $\delta_0 = \phi/(\phi + g_n V_c)$  where  $g_n$  is a constant [18]. This has an additional benefit of assuring  $(d^2 I_d / dV_{ds}^2)_{V_{ds}=0} = 0$  which is an important manifestation of the model symmetry (violated in  $V_{th}$ -based models) [12].

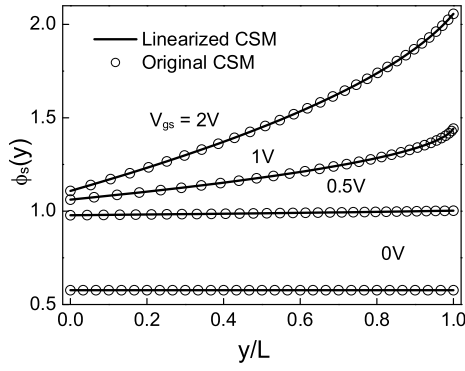


Fig. 3. Surface potential along the channel computed from the original (circles) and symmetrically linearized CSM (solid lines);  $t_{ox} = 25\text{\AA}$ ,  $N_{sub} = 5 \times 10^{17}\text{cm}^{-3}$ ,  $V_{fb} = -0.8\text{V}$ ,  $\mu = 400\text{cm}^2/\text{V}\cdot\text{s}$ ,  $V_{ds} = 1\text{V}$  and  $V_{sb} = 0\text{V}$

Similarly, the explicit  $\phi_s(y)$  dependence can be obtained

$$\phi_s(y) = \phi_m + H \left[ 1 - \sqrt{1 - (2\phi/HL)(y - y_m)} \right] \quad (7)$$

where  $y_m = (L/2)(1 + \phi/4H)$  is the coordinate of the potential midpoint ( $\phi_s(y_m) = \phi_m$ ) and  $H = [(q_{im}/\alpha) + \phi_t](1 + \delta_0\phi/r_L V_c)^{-1}$ .

Comparison of (7) with the more complicated CSM result (for a special case of no velocity saturation) is shown Fig. 3 further verifying the symmetric linearization concept.

This simplification of the  $\phi_s(y)$  dependence leads to computationally efficient expressions for the terminal charges (all normalized to  $WLC_{ox}$ ). For example, the gate charge

$$Q_G = \int_{\phi_{ss}}^{\phi_{sd}} (V_{gb} - V_{fb} - \phi_s)(dy/d\phi_s)d\phi_s \quad (8)$$

becomes

$$Q_G = V_{gb} - V_{fb} - \phi_m + (\eta_p\phi/2)(r_L\phi/6H - 1 + r_L) \quad (9)$$

Here  $\eta_p$  describes the polysilicon depletion effect ( $\eta_p = 1$  when poly depletion is neglected). Similarly, it is easy to implement the Ward-Dutton partition [21] to obtain

$$|Q_D| = \frac{q_{im}}{2} + \frac{\alpha\phi}{12} \left( 1 - \frac{\phi}{2H} - \frac{\phi^2}{20H^2} \right) \quad (10)$$

and the remaining charges  $Q_B$  and  $Q_S$ . In [17], these expressions we verified by comparison with exact results [22] which are too complex for compact modeling purposes. An important feature of SP is that (9) remains valid in the accumulation region. Typical C-V curves are shown in Fig. 4.

A physics-based description of the accumulation region (unique to a  $\phi_s$ -based approach) allows MOS varactor modeling, illustrated in Fig. 5 by evaluating the tuning range of the voltage-controlled oscillator (VCO) shown in Fig. 6. SP also includes a more detailed MOS varactor model based on the relaxation approximation for the formation of the MOSFET inversion channel [23].

The symmetry of SP is illustrated in Fig. 7 and enables accurate modeling of the R2R circuit shown in Fig. 8. Typical results are shown in Fig. 9. As noted by the EKV group, the latter is problematic for  $V_{th}$ -based models [24]. SP verification is based on comparison with the experimental data

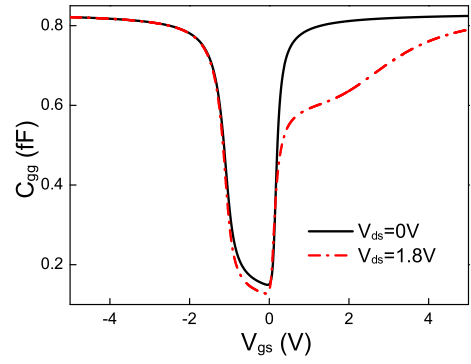


Fig. 4. Typical C-V curves for  $W = 0.5\mu\text{m}$ ,  $L = 0.15\mu\text{m}$  device;  $t_{ox} = 40\text{\AA}$ ,  $N_{sub} = 5 \times 10^{17}\text{cm}^{-3}$  and  $V_{fb} = -1.1\text{V}$

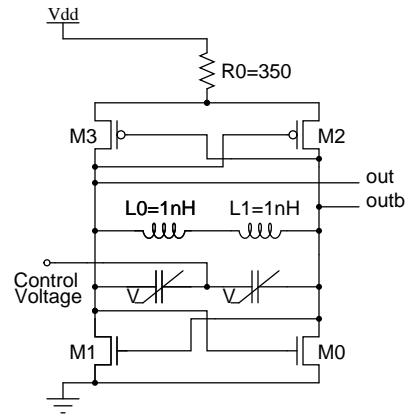


Fig. 5. Voltage controlled oscillator

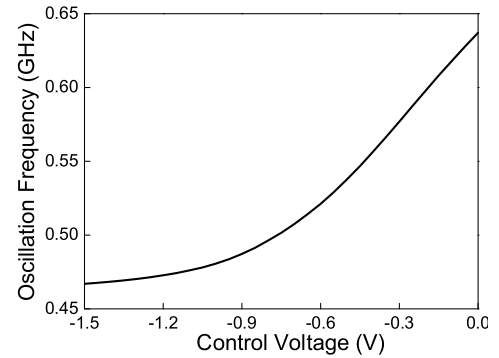


Fig. 6. Tuning range of the voltage controlled oscillator;  $t_{ox} = 42\text{\AA}$ ,  $N_{sub} = 6.5 \times 10^{17}\text{cm}^{-3}$  and  $V_{fb} = 1.0\text{V}$  (p-channel varactors)

for several fabrication processes from different manufacturers. Typical results are shown in Fig. 10. Further details of SP including the symmetry of charges and transcapacitances are discussed in [13], [25]. The  $\phi_s$ -based description of quantum and polysilicon depletion effects can be found in [26], [27].

## Overlap Charge

The bias dependence of the overlap charge is essential for transient simulation of MOSFET circuits [28]. This is particularly important in scaled devices where the overlap regions occupy a significant fraction of the gate length. Physically, the

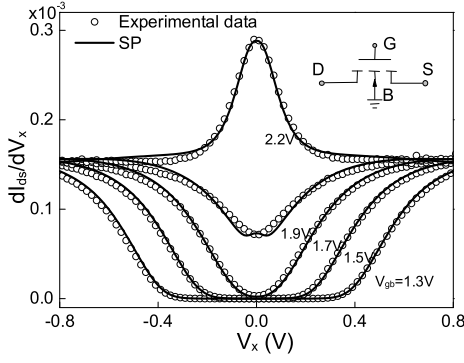


Fig. 7. Gummel Symmetry Test;  $W = 0.245\mu\text{m}$ ,  $L = 0.196\mu\text{m}$ ;  $V_S = V_{b0} - V_x$ ,  $V_D = V_{b0} + V_x$ ,  $V_{b0} = 1\text{V}$

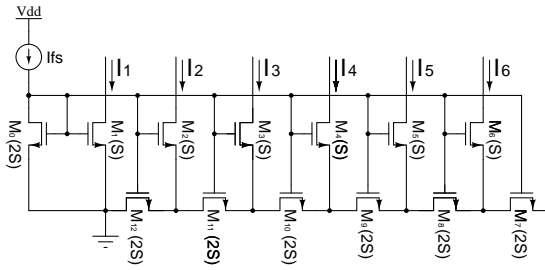


Fig. 8. R2R circuit

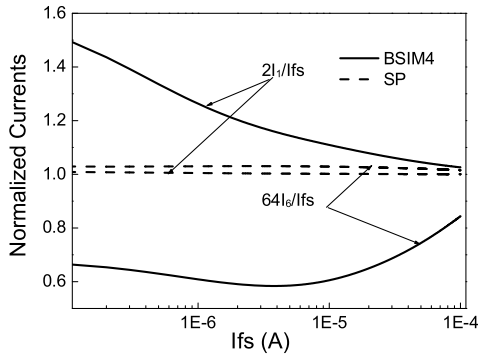


Fig. 9. Simulation results for R2R circuit

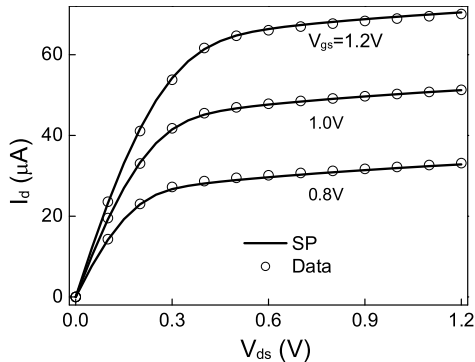


Fig. 10. Output characteristics of MOSFET with  $W = 0.12\mu\text{m}$ ,  $L = 0.1\mu\text{m}$

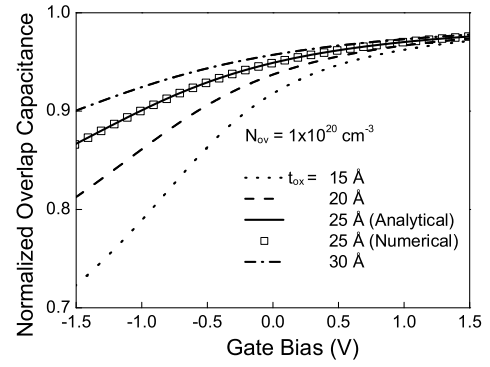


Fig. 11. Comparison of normalized overlap capacitance with numerical solution

overlap region can be modeled as a MOS capacitor [28], [29]:

$$Q_{ov} = C_{ox} W L_{ov} (V_g - \phi_{ov}) \quad (11)$$

where  $V_g$  is either  $V_{gs}$  or  $V_{gd}$  and  $L_{ov}$  is the overlap length. As shown in Fig. 11, an analytical approximation for  $\phi_{ov}$  results in excellent agreement with numerical calculations for  $C_{ov} = dQ_{ov}/dV_g$ .

### Gate Tunneling Current

Aggressive scaling of  $t_{ox}$  necessitates accurate compact modeling of the gate tunneling current,  $I_g$ . SP includes a novel compact model of  $I_g$  which is valid in all regions of operation and is  $\phi_s$ -based in both the channel and the overlap regions. The total gate current is a sum of the contributions from the overlap regions ( $I_{gov}$ ) and from the channel area ( $I_{gc}$ ). For each component the model has identical functional form and parameter values. Physical modeling of the overlap components is important since they dominate for small gate biases (where the oxide field in the overlap regions is larger than that in the channel area) and contribute a significant fraction of  $I_g$  in scaled devices where the overlap region is geometrically comparable to the channel area. The physical result  $I_g = 0$  for  $V_{gs} = V_{ds} = 0$  is achieved by employing the Esaki-Tsu supply function,  $F_s$ , to describe the difference of carrier populations across the gate oxide. For each component, the tunneling current density [30]

$$J_g = J_0 F_s \exp \left\{ -B_0 \left[ G_1 + G_2 \frac{|V_{ox}|}{\chi_B} + G_3 \left( \frac{V_{ox}}{\chi_B} \right)^2 \right] \right\} \quad (12)$$

which is derived by simplifying the Esaki-Tsu integral [31]. In (12)  $J_0$  and  $B_0$  are physical constants,  $V_{ox}$  is the oxide voltage,  $q\chi_B$  is the conduction band offset at the Si/SiO<sub>2</sub> interface,

$$F_s = \ln \left\{ \frac{1 + \exp[(\phi_s - \phi_n - \alpha_b - \psi_t)/\phi_t]}{1 + \exp[(\phi_s - V_{gb} - \alpha_b - \psi_t)/\phi_t]} \right\}, \quad (13)$$

where  $q\alpha_b$  is the difference between the conduction band edge and the Fermi level in the Si bulk, and

$$\psi_t = (1/2) \left[ \sqrt{(V_{ox} - G_0 \phi_t)^2 + 0.01} - (V_{ox} - G_0 \phi_t) \right]. \quad (14)$$

is the bias-dependent tunneling energy relative to the conduction band edge at the Si/SiO<sub>2</sub> interface. In (12) and (14), the model parameters  $G_0, \dots, G_3$  are used to include the possible conduction band misalignment between Si and polysilicon, to absorb the uncertainties of the effective mass of electrons and the band offset, and to compensate the numerical error introduced by using the WKB approximation.

As a result of the negligible position dependence of  $J_g$  in the overlap regions,  $I_{gs(ov)}$  and  $I_{gd(ov)}$ , are obtained directly

$$I_{gs(d)ov} = WL_{ov}J_g(V_{gs(d)}). \quad (15)$$

The  $V_{ds}$  dependence of  $I_{gc}$  and its partition into the source ( $I_{gcs}$ ) and drain ( $I_{gcd}$ ) components are modeled using the approach given in [32],

$$I_{gc} = W \int_0^L J_g(y) dy, \quad (16)$$

$$I_{gcd} = W \int_0^L J_g(y) (y/L) dy, \quad (17)$$

and  $I_{gcs} = I_{gc} - I_{gcd}$ . Using a symmetric linearization method the integrals are readily evaluated in closed form. The accuracy of the  $I_g$  model has been verified using experimental data for two advanced CMOS processes [30]. Typical results are shown in Figs. 12 – 14. Due to physical modeling of the overlap region contributions, no scaling parameters are necessary to provide an accurate fit for devices with different geometries.

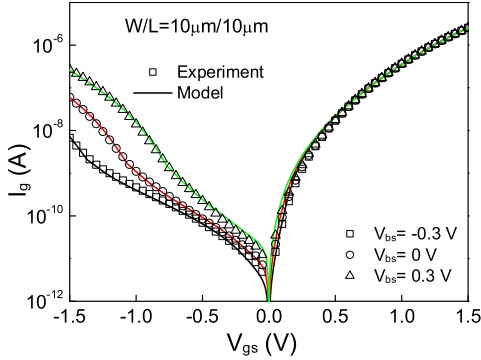


Fig. 12.  $I_g$  model verification for long-channel device;  $V_{ds} = 0$

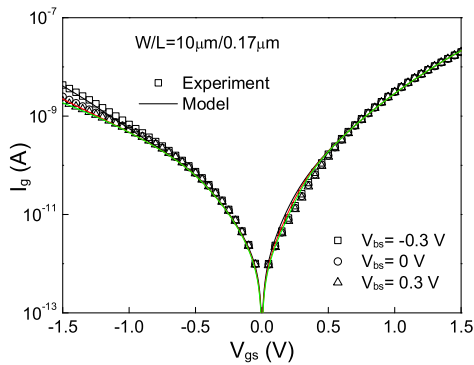


Fig. 13.  $I_g$  model verification for short-channel device;  $V_{ds} = 0$

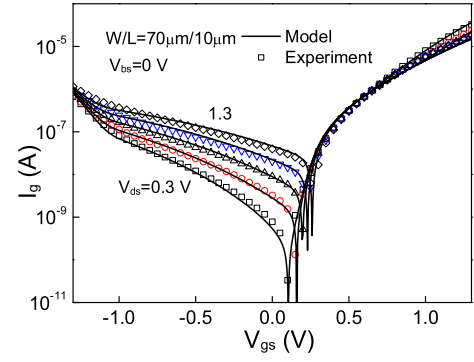


Fig. 14.  $I_g(V_{ds})$  model verification.

### Substrate Current

The availability of the surface potential also simplifies the formulation of the substrate current model. The latter is usually obtained by modifying the expression given in [33]

$$I_b = I_d b_1 (V_{ds} - b_3 V_{dsat}) \exp\left(-\frac{b_2}{V_{ds} - b_3 V_{dsat}}\right), \quad (18)$$

where  $b_1, b_2$  and  $b_3$  are geometry dependent, and  $V_{dsat}$  is the saturation voltage. Although accurate in the strong inversion region, expression (18) is not suitable for the subthreshold region where [34]

$$I_b = I_d b_1 \exp(-b_2/V_{ds}). \quad (19)$$

Most of the existing compact models rely on smoothing functions to achieve a transition between (18) and (19). In SP the same result is achieved by replacing  $V_{dsat}$  with  $\phi$ :

$$I_b = I_d b_1 \exp[-b_2/(V_{ds} - b_3 \phi)] \quad (20)$$

In the subthreshold region  $\phi$  is exponentially small and (19) is recovered as a particular case of (20). In the strong inversion region,  $V_{ds} - \phi$  represents the potential drop across the velocity saturation region which is equivalent to  $V_{ds} - V_{dsat}$  in the context of  $V_{th}$ -based models [33]; consequently (20) is equivalent to (18).

Further details including scaling and comparison with experimental data can be found in [35].

### Noise

SP includes the channel thermal noise, channel flicker noise, channel-induced gate noise, and series resistance noise.

For the channel thermal noise, the excess noise in short-channel devices is modeled via the channel length modulation (CLM) effect. The power spectral density of the channel thermal noise is [36]

$$S_{id} = (4kT/L_{red}^2) \mu Q_{inv} + \delta_{HE} (4kT/L_{red}^2 E_c^2) I_d \phi \quad (21)$$

where  $L_{red}$  is the CLM reduced channel length and  $Q_{inv}$  is the inversion charge in the gradual channel region. The second term describing the “hot electron” noise is included in SP for legacy purposes but is not needed in most cases [36], [37].

The SP flicker noise model is obtained by developing a  $\phi_s$ -based version of the model in [38], which includes fluctuations

of both the effective mobility and of the number of mobile carriers ( $N$ ). The spectral density at frequency  $f$  is given by

$$S_{id} = \frac{kTI_d^2}{\gamma_{FN}WL_{red}^2f^{NEF}} \int_0^{L_{red}} \frac{A + BN + CN^2}{(N + N_*)^2} dy, \quad (22)$$

where  $N_* = (C_{ox}\phi_t/q)(1 + \gamma/\sqrt{\phi_m + 10^{-6}\phi_t})$ ,  $\gamma_{FN} = 10^{10}\text{m}^{-1}$  is a physical constant and  $A$ ,  $B$ ,  $C$  and  $NEF$  are technology-dependent parameters.

In (22), the contribution to the velocity saturation region is neglected based on the same argument as the one leading to (21) [36], [37]. Symmetric linearization yields

$$dy/dN = (\mu Wq/\alpha_m C_{ox} I_d) (qN + \alpha_m \phi_t C_{ox}), \quad (23)$$

and the integral in (22) is readily evaluated in a closed form:

$$S_{id} = S_{id}^{\text{drift}} + S_{id}^{\text{diff}}. \quad (24)$$

The two terms in (24) represent the contributions of the drift and diffusion currents, respectively. The drift term

$$S_{id}^{\text{drift}} = \frac{q^2 kT \mu I_d}{\gamma_{FN} \alpha_m L_{red}^2 C_{ox} f^{NEF}} \left[ C (N_0^2 - N_L^2) / 2 + (B - 2CN_*) (N_0 - N_L) - (AN_* - BN_*^2 + CN_*^3) (N_0 - N_L) / (N_1 N_2) + (A - 2BN_* + 3CN_*^2) \ln (N_1 / N_2) \right] \quad (25)$$

is dominant in the strong inversion region whereas the diffusion term

$$S_{id}^{\text{diff}} = \frac{k^2 T^2 \mu I_d}{\gamma_{FN} L_{red}^2 f^{NEF}} \left[ C (N_0 - N_L) + (B - 2CN_*) \ln (N_1 / N_2) + (A - BN_* + CN_*^2) (N_0 - N_L) / (N_1 N_2) \right] \quad (26)$$

dominates in the subthreshold region. In (25) and (26),  $N_1 = N_0 - N_*$ ,  $N_2 = N_L - N_*$ , where  $N_0$  and  $N_L$  are the number of mobile carriers at the source and drain end of the gradual channel, respectively. One of the advantages of the  $\phi_s$ -based formulation is a single expression for  $S_{id}$  valid in all regions of operation. This obviates the need for smoothing functions or interpolating formulas inevitable in  $V_{th}$ -based formulations.

The application of the SP noise model to the phase noise simulation of the VCO shown in Fig. 5 is illustrated in Fig. 15. As explained in [39], flicker noise is responsible for the 30dBc/dec slope in the close-in sideband.

### Large Signal NQS Model

Accurate analysis of fast transients requires CAD-compatible large-signal NQS models of MOSFETS. A standard approach is to use channel segmentation, which works well when skillfully implemented, but requires considerable effort on the part of the user and numerous additional node points during circuit simulation [40]. A physically based alternative is to use the partial differential equation [41]:

$$\frac{\partial q_i}{\partial t} + \frac{\partial}{\partial y} \left[ \left( \frac{q_i}{dq_i/d\phi_s} - \phi_t \right) \frac{\partial q_i}{\partial y} \right] = 0. \quad (27)$$

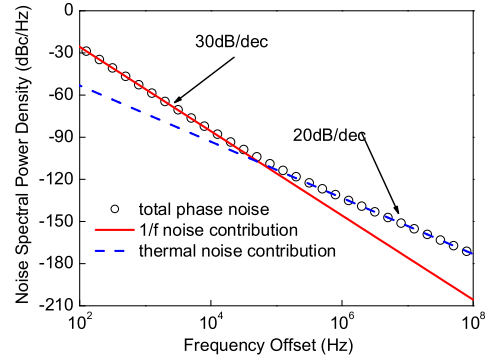


Fig. 15. Free-Running Oscillator Phase Noise Simulation

In this section, we use the physical sign of  $q_i$ , variables  $y$  and  $t$  are normalized to  $L$  and  $L^2/\mu$ , respectively, currents are normalized to  $\beta$  and the integrated terminal charges are normalized to  $WLC_{ox}$ . Numerical solution is straightforward but is too inefficient for the compact modelling purposes. The standard approach is to solve (27) approximately using a weighted residuals method [42], [43]. The collocation version of this method is most physical and is readily implemented in circuit simulators [44]. The drawback is its limited accuracy since the use of high degree polynomials for the approximate inversion charge  $\tilde{q}_i$  results in unphysical oscillations of  $\tilde{q}_i$  as a function of distance. To overcome this difficulty, the SP NQS model uses a spline collocation method. For two collocation points:

$$\tilde{q}_i = \begin{cases} \tilde{q}_0 + (3\tilde{q}_{1/3} - 3\tilde{q}_0 + 3a_0)y + (3a_1 - 9a_0)y^2 - 9a_1y^3, & 0 \leq y \leq 1/3 \\ 2\tilde{q}_{1/3} - \tilde{q}_{2/3} - 2a_2 + (3\tilde{q}_{2/3} - 3\tilde{q}_{1/3} + 9a_2 - 2a_3)y + (9a_3 - 9a_2)y^2 - 9a_3y^3, & 1/3 \leq y \leq 2/3 \\ 3\tilde{q}_{2/3} - 2\tilde{q}_1 - 6a_4 + (3\tilde{q}_1 - 3\tilde{q}_{2/3} + 15a_4 - 6a_5)y + (15a_5 - 9a_4)y^2 - 9a_5y^3, & 2/3 \leq y \leq 1 \end{cases} \quad (28)$$

This converts (27) into a system of two ordinary differential equations

$$d\tilde{q}_{1/3}/dt + \varphi(\tilde{q}_{1/3})\nu_1^2 + \psi(\tilde{q}_{1/3})\nu_2 = 0, \quad (29)$$

$$d\tilde{q}_{2/3}/dt + \varphi(\tilde{q}_{2/3})\nu_3^2 + \psi(\tilde{q}_{2/3})\nu_4 = 0, \quad (30)$$

where  $\tilde{q}_{1/3} = \tilde{q}(1/2, t)$ ,  $\tilde{q}_{2/3} = \tilde{q}(2/3, t)$

$$\varphi(q_i) = q_b q_i / (q_b - \gamma^2/2) - \phi_t, \quad (31)$$

$$\psi(q_i) = \frac{q_b}{q_b - \gamma^2/2} - \frac{\gamma^4 q_i}{4(q_i - \gamma^2/2)^3} \quad (32)$$

$$\nu_1 = (-7\tilde{q}_0 - 3\tilde{q}_{1/3} + 12\tilde{q}_{2/3} - 2\tilde{q}_1)/5 \quad (33)$$

$$\nu_2 = 18(4\tilde{q}_0 - 9\tilde{q}_{1/3} + 6\tilde{q}_{2/3} - \tilde{q}_1)/5 \quad (34)$$

$$\nu_3 = (2\tilde{q}_0 - 12\tilde{q}_{1/3} + 3\tilde{q}_{2/3} + 7\tilde{q}_1)/5 \quad (35)$$

and

$$\nu_4 = 18(-\tilde{q}_0 + 6\tilde{q}_{1/3} - 9\tilde{q}_{2/3} + 4\tilde{q}_1)/5 \quad (36)$$

The ordinary differential equations can be solved simultaneously using subcircuit techniques inside the simulator (included as a part of SP; no effort is required from the user). After  $\tilde{q}_i$  is determined, the terminal currents are evaluated as in [41] to obtain  $i_G = i_S - i_D - i_B$  where

$$i_S = I - \frac{11}{91} \frac{d\tilde{q}_0}{dt} - \frac{4}{15} \frac{d\tilde{q}_{1/3}}{dt} - \frac{1}{10} \frac{d\tilde{q}_{2/3}}{dt} - \frac{1}{90} \frac{d\tilde{q}_1}{dt} \quad (37)$$

$$i_D = I + \frac{1}{90} \frac{d\tilde{q}_0}{dt} + \frac{1}{10} \frac{d\tilde{q}_{1/3}}{dt} + \frac{4}{15} \frac{d\tilde{q}_{2/3}}{dt} + \frac{11}{90} \frac{d\tilde{q}_1}{dt} \quad (38)$$

$$i_B = \frac{1}{6} \left[ \frac{d\tilde{q}_b(0,t)}{dt} + 4 \frac{d\tilde{q}_b(1/2,t)}{dt} + \frac{d\tilde{q}_b(1,t)}{dt} \right] \quad (39)$$

and  $I$  is given by the stationary equation (6) for the drain current, but with the actual time-dependent terminal voltages.

Typical simulation results are shown in Fig. 16 and Fig. 17, and illustrate the accuracy of the spline collocation method. The main advantage of the spline implementation of the collocation method is that the number of collocation points (equal to the number of ordinary differential equations which one needs to solve) can be arbitrarily high or low providing the circuit designer with an easy trade-off between accuracy and efficiency of simulation.

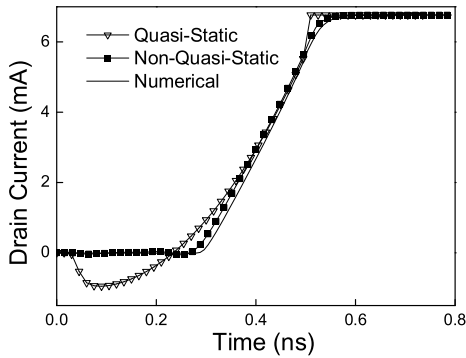


Fig. 16. Comparison of drain currents computed using quasi-static, non-quasi-static approximations and numerical calculations.  $V_{ds} = 5V$ .  $V_{gs}$  changes from 0 to 5V at a ramp rate  $10^{10}V/s$ .

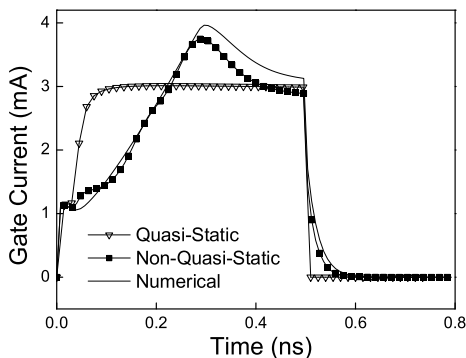


Fig. 17. Comparison of gate currents computed using quasi-static, non-quasi-static approximations and numerical calculations.  $V_{ds} = 5V$ .  $V_{gs}$  changes from 0 to 5V at a ramp rate  $10^{10}V/s$ .

## Quasi-Ballistic Transport

Scaling of the channel length below 100nm in either traditional or double-gate MOSFETs may require inclusion of the quasi-ballistic transport in a compact MOSFET model. This is a difficult task, but S-matrix techniques [45] provide a framework which is sufficiently simple for compact modeling purposes. The S-matrix of a non-absorbing barrier can be evaluated as long as its potential profile is known [46] making  $\phi_s$ -based formulation particularly well suited for sub 100nm MOSFET modeling. The synthesis of SP with the S-matrix method has been demonstrated to provide a model which is sufficiently simple for circuit simulation purposes and provides a gradual transition from drift-diffusion to ballistic transport as  $L$  becomes comparable to the mean free path [47].

## Conclusions

The structural advantages of  $\phi_s$ -based models together with the rapid progress in the development and implementation of this approach make it a most promising platform for the next generation of compact MOSFET models. When combined with a one-flux description of quasi-ballistic effects it is likely to provide efficient and physical modeling of MOS transistors in the foreseeable future.

## Acknowledgments

This work is supported in part by the Semiconductor Research Corporation (contracts numbers 2000-NJ-796 and 2000-NJ-997). We are grateful to P. Bendix, D. Foty, W. Grabinski, L. Leimatre, C. McAndrew, S. Shapira, S. Veeraraghavan, J. Victory and G. Workman for their help with various aspects of model development including the experimental data shown above.

## REFERENCES

- [1] W. Liu, *MOSFET models for SPICE simulation including BSIM3v3 and BSIM4* (Wiley, New York, 2001)
- [2] D. Foty, *MOSFET modeling with SPICE: principles and practice* (Prentice Hall PTR, Upper Saddle River, NJ 1997)
- [3] M.A. Maher and C.A. Mead, *Advanced Reserach in VLSI* (MIT Press, Cambridge, MA, 1987)
- [4] Y.H. Byun, K. Lee and M. Shur, *IEEE Electron Device Lett.*, **11**, 50 (1991)
- [5] C. Enz, F. Krummenacher and E.A. Vittoz, *Analog Integrated Circuits and Signal Processing Journal*, **8**, 83 (1995)
- [6] A.I.A. Cunha, M.C. Schneider and C. Galup-Montoro, *Solid-State Electron*, **38**, 1945 (1995)
- [7] J.-M. Sallese, M. Bucher, F. Krummenacher and P. Fazan, *Solid-State Electronics*, **47**, 677 (2003)
- [8] H.K. Gummel, *IEEE Trans. Electron Devices*, **48**, 1585 (2001)
- [9] J. He, X. Xi, M. Chan, A. Niknejad and C. Hu, *Tech. Proc. ICMSM2003*, 266 (2003)
- [10] M. Miura-Mattausch, U. Feldmann, A. Rahm, M. Bollu and D. Savignac, *IEEE Trans Computer-Aided Des.*, **15**, 1 (1996)
- [11] R. van Langevelde and F.M. Klaassen, *Solid-State Electronics*, **44**, 409 (2000)
- [12] K. Joardar, K.K. Gullapalli, C.C. McAndrew, M.E. Burnham and A. Wild, *IEEE Trans. Electron Devices*, **45**, 134 (1998)
- [13] T.-L. Chen and G. Gildenblat, *Tech. Proc. ICMSM2002*, 657 (2002)
- [14] H.C. Pao and C.T. Sah, *Solid-State Electronics*, **9**, 927 (1966)
- [15] J.R. Brews, *Solid-State Electronics*, **21**, 345 (1978)

- [16] C. Turchetti and G. Masetti, *IEEE Trans. Computer-Aided Des., CAD-3*, 117 (1984)
- [17] T.-L. Chen and G. Gildenblat, *Solid-State Electronics*, **45**, 335 (2001)
- [18] N.D. Arora, *MOSFET models for VLSI circuit simulation* (Springer-Verlag, New York, 1993)
- [19] T.-L. Chen and G. Gildenblat, *Electronics Letters*, **37**, 791 (2001)
- [20] T. Grotjohn and B. Hoefflinger, *IEEE J. Solid-State Circuits*, **19**, 100 (1984)
- [21] D.E. Ward and R.W. Dutton, *IEEE J. Solid-State Circuits*, **13**, 703 (1978)
- [22] C.C. McAndrew and J. Victory, *IEEE Trans. Electron Devices*, **49**, 72 (2002)
- [23] J. Victory, C.C. McAndrew and K. Gullapalli, *IEEE Electron Device Letters*, **22**, 245 (2001)
- [24] M. Bucher, *École Polytechnique Fédérale de Lausanne, Thèse N°2114* (1999)
- [25] P. Bendix, *Tech. Proc., IMSM2002*, 649 (2002)
- [26] G. Gildenblat, T. L. Chen and P. Bendix *IEEE Electronics Letters*, **35**, 1974 (1999)
- [27] G. Gildenblat, T. L. Chen and P. Bendix *IEEE Electronics Letters*, **36**, 1072 (2000)
- [28] P. Klein, K. Hoffmann and B. Lemaitre, *IEDM Tech. Dig.*, 493 (1993)
- [29] R. van Langevelde, "Model Summary of MOS11", <http://www.semiconductors.philips.com/philipsmodels>
- [30] X. Gu, G. Gildenblat, G. Workman, S. Veeraraghavan, S. Shapira and K. Stiles, *Tech. Proc. ICMCM2003*, 318 (2003)
- [31] R. Tsu and L. Esaki, *Appl. Phys. Lett.*, **22**, 562 (1973)
- [32] W-K Shih, R. Rios, P. Packan, K. Mistry and T. Abbott, *IEDM Tech. Dig.*, 293 (2001)
- [33] C. Hu, S.C. Tam, F.C. Hsu, P.K. Ko, T.Y. Chan and and K.W. Terrill, *IEEE Trans. Electron Devices*, **32**, 375 (1985)
- [34] B. Iniguez and T.A. Fjeldly, *Solid-State Electronics*, **41**, 87 (1997)
- [35] X. Gu, H. Wang, T.L. Chen and G. Gildenblat, *Tech. Proc. ICMCM2003*, 310 (2003)
- [36] C.-H. Chen and M.J. Deen, *IEEE Trans. Electron Devices*, **49**, 1484 (2002)
- [37] A.J. Scholten, L.F. Tiemeijer, R. van Langevelde, R.J. Havens, V.C. Venezia, A.T.A. Zegers-van Duijnhoven, B. Neinhuis, C. Jungemann and D.B.M. Klaasen, *IEDM Tech. Dig.*, 129 (2002)
- [38] K.K. Hung, P.K. Ko, C. Hu and Y.C. Cheng, *IEEE Trans. Electron Devices*, **37**, 654 (1990)
- [39] A. Hajimiri and T.H. Lee, *IEEE J. Solid-State Circuits*, 179 (1998)
- [40] A.J. Scholten, L.F. Tiemeijer, P.W.H. de Vreede and D.B.M. Klaassen, *IEDM Tech. Dig.*, 163 (1999)
- [41] P. Mancini, C. Turchetti and G. Masetti, *IEEE Trans. Electron Devices*, **ED-34**, 325 (1987)
- [42] C. Turchetti, P. Mancini and G. Masetti, *IEEE J. Solid-State Circuits*, **SC-21**, 827 (1986)
- [43] W. Liu, C. Bowen and M. Chang, *IEDM Tech. Dig.*, 151 (1996)
- [44] D.H. Kwon, Y.S. Yu, K.H. Kim, T.-W. Yeon and S.W. Hwang, *J. Korean Physical Soc.*, **33**, 192 (1998)
- [45] Z. Ren and M.S. Lundstrom, *Superlattices and Microstructures*, **27**, 179 (2000)
- [46] G. Gildenblat, *J. Appl. Phys.*, **91**, 9883 (2002)
- [47] H. Wang and G. Gildenblat, *IEDM Tech. Digest*, 125 (2002)

## Appendix A: Surface Potential Approximation

Below

$$x_g = (V_{gb} - V_{fb})/\phi_t, \quad (A1)$$

$$G = \gamma/\sqrt{\phi_t}, \quad (A2)$$

$$\xi = 1 + G/\sqrt{2}, \quad (A3)$$

$$x_{g23} = G\sqrt{x_{23} - 1}, \quad (A4)$$

$$x_{23} = \begin{cases} (\phi_b + V_{sb})/\phi_t & \text{for } V_{sb} \geq 0 \\ (\phi_b + 0.5V_{sb})/\phi_t & \text{for } V_{sb} < 0 \end{cases} \quad (A5)$$

$$\text{MINA}(a, b, c) = \left[ a + b - \sqrt{(a-b)^2 + c} \right] / 2, \quad (A6)$$

$$\sigma(a, c, \tau) = \frac{a(a+c)}{u + c(a+c)(c^2/3 - a)/u}, \quad (A7)$$

and

$$u = v^2/\tau + c^2/2 - a \quad (A8)$$

The algorithm for non-iterative computation of the surface potential is as follows. For  $x_g < 0$ , denote  $y_g = -x_g$ ,  $z = 5y_g/4\xi$  and proceed in the following steps

$$\eta = (1/2) \left\{ z + 10 - [(z-6)^2 + 64]^{1/2} \right\} \quad (A9)$$

$$a = (y_g - \eta)^2 + G^2(\eta + 1) \quad (A10)$$

$$c = 2(y_g - \eta) - G^2 \quad (A11)$$

$$\tau = -\eta + \ln(a/G^2) \quad (A12)$$

$$y_0 = \eta + \sigma(a, c, \tau) \quad (A13)$$

$$\Delta_0 = \exp(y_0); \Delta_1 = 1/\Delta_0 \quad (A14)$$

$$p = 2(y_g - y_0) + G^2[\Delta_0 - 1 + \Delta_n(2 - \Delta_0 - \Delta_1)] \quad (A15)$$

$$q = (y_g - y_0)^2 + G^2[y_0 - \Delta_0 + 1 + \Delta_n(\Delta_0 - \Delta_1 - 2y_0)] \quad (A16)$$

$$x = -y_0 - \frac{2q}{p + \sqrt{p^2 - 2q\{2 - G^2[\Delta_0 + \Delta_n(\Delta_1 - \Delta_0)]\}}} \quad (A17)$$

For  $0 < x_g < x_{g23}$  compute

$$\bar{x} = (x_g/\xi)[1 + x_g(\xi x_{23} - x_{g23})/x_{g23}^2] \quad (A18)$$

$$\bar{E} = \exp(-\bar{x}) \quad (A19)$$

$$\omega = 1 - \bar{E} - \Delta_n(\bar{E}^{-1} - \bar{E} - 2\bar{x}) \quad (A20)$$

$$x_0 = x_g + G^2/2 - G(x_g + G^2/4 - \omega)^{1/2} \quad (A21)$$

$$\Delta_0 = \exp(x_0); \Delta_1 = 1/\Delta_0 \quad (A22)$$

$$p = 2(x_g - x_0) + G^2[1 - \Delta_1 + \Delta_n(\Delta_0 + \Delta_1 - 2)] \quad (A23)$$

$$q = (x_g - x_0)^2 - G^2[x_0 + \Delta_1 - 1 + \Delta_n(\Delta_0 - \Delta_1 - 2x_0)] \quad (A24)$$

and

$$x = x_0 + \frac{2q}{p + \sqrt{p^2 - 2q\{2 - G^2[\Delta_1 + \Delta_n(\Delta_0 - \Delta_1)]\}}} \quad (A25)$$

Finally, for  $x_g > x_{g23}$  (A22)-(A25) remain unchanged, but instead of (A21)  $x_0$  is computed as follows:

$$x_{\text{sub}} = x_g + G^2/2 - G(x_g + G^2/4 - 1)^{1/2} \quad (A26)$$

$$\eta = \text{MINA}(x_{\text{sub}}, x_n + 3, 5) \quad (A27)$$

$$a = (x_g - \eta)^2 - G^2\eta + G^2 \quad (A28)$$

$$c = 2(x_g - \eta) + G^2 \quad (A29)$$

$$\tau = x_n - \eta + \ln(a/G^2) \quad (A30)$$

$$x_0 = \eta + \sigma(a, c, \tau) \quad (A31)$$

To reduce the numerical noise for  $V_{gb}$  close to  $V_{fb}$  it may be useful to code  $x = x_g/\xi$  for  $|x| < 10^{-7}\xi$ .